PhotoScience Advances
https://www.sciltp.com/journals/psa

Article

Ultrafast Electron Transfer from Higher Excited States in Perylene Monoimide—Nanocrystal Hybrids Revealed by Pump-Push-Probe Spectroscopy

Mizuki Sato [1], Daisuke Yoshioka [1], Hikaru Sotome [2], Yuki Nagai [1] and Yoichi Kobayashi [1,*]

[1] Department of Applied Chemistry, College of Life Sciences, Ritsumeikan University, Kusatsu 525-8577, Shiga, Japan
[2] Division of Frontier Materials Science and Center for Advanced Interdisciplinary Research, Graduate School of Engineering Science, The University of Osaka, Toyonaka 565-0871, Osaka, Japan
* Correspondence: ykobayas@fc.ritsumei.ac.jp

How To Cite: Sato, M.; Yoshioka, D.; Sotome, H.; et al. Ultrafast Electron Transfer from Higher Excited States in Perylene Monoimide—Nanocrystal Hybrids Revealed by Pump-Push-Probe Spectroscopy. *PhotoScience Advances* **2026**, *1*(1), 4.

Received: 17 April 2026
Revised: 20 May 2026
Accepted: 5 June 2026
Published: 7 June 2026

Abstract: Higher excited states are attractive for driving high-energy photochemistry, but their ultrafast relaxation usually prevents direct utilization. Here we demonstrate, by pump-push-probe spectroscopy, ultrafast electron injection from higher excited states of perylene monoimide (PMI) coordinated to CdS and ZnS nanocrystals (NCs). Despite the weak electronic interaction between the lowest excited state of PMI and the NC surface, sequential excitation with 520 and 650 nm pulses generates long-lived charge-separated states through higher excited-state electron injection. A modified subtraction analysis disentangles the genuine higher excited-state dynamics from apparent population change of the lowest excited state, revealing sub-picosecond interfacial electron transfer and enhanced PMI radical anion formation in the ZnS system. This work establishes PMI-NC hybrids as a platform for harvesting short-lived high-energy excited states as long-lived reactive charges under visible light.

Keywords: pump-push-probe spectroscopy; perylene monoimide; higher excited-state; nanocrystals; electron transfer

1. Introduction

Harnessing visible and near-infrared light to drive high-energy reactions is a central challenge in photochemistry and materials chemistry [1–3]. Achieving this goal would enable highly selective photochemical transformations under mild conditions and precise spatiotemporal control in condensed-phase systems. One promising approach to overcome this limitation is stepwise two-photon excitation, in which two photons are sequentially absorbed via a real intermediate excited state [4–6]. Compared with simultaneous two-photon absorption, stepwise two-photon excitation can be achieved at much lower excitation intensities, yet still enables access to higher excited states or excited states of transient species under visible or near-infrared light. Accordingly, it has been applied to photocatalytic reactions utilizing high redox properties [7–13], optical switching [14–17], triplet–triplet annihilation upconversion [18–21], photoinitiators for 3D laser nanoprinting [22–24] and photoionization [25–27].

On the other hand, higher excited states accessed by stepwise two-photon excitation generally undergo ultrafast relaxation in accordance with Kasha's rule, and their lifetimes are often limited to the sub-picosecond or picosecond regime [28,29]. As a result, it is difficult to directly utilize these states for intermolecular chemical reactions. This has become a fundamental challenge that limits the general applicability of this approach. Recently, a strategy has been proposed to overcome this short-lifetime problem by ultrafast extraction of the high-energy electron to an inorganic material, thereby extending its lifetime [30]. For example, in perylene bisimide (PBI)-based systems, it has been demonstrated that higher excited-state electrons generated by stepwise two-photon

excitation can be injected into the conduction band of inorganic nanocrystals (NCs), resulting in a lifetime that is orders of magnitude longer than that of the higher excited state of the molecule alone [31–33]. Accordingly, a design principle is emerging in which short-lived high-energy electrons are converted into reactive states with lifetimes long enough to be utilized in chemical reactions.

However, previous proof-of-concept studies have been largely limited to PBI frameworks. Extending this concept to perylene monoimide (PMI) is particularly important because the reduced number of imide substituents shifts its electronic levels to more negative potentials, potentially enabling access to more strongly reducing excited states. Clarifying whether the concept of lifetime prolongation through the extraction of electrons from higher excited states, established for PBI systems, can also be applied to PMI systems is essential for building a general framework for designing photoreactions that exploit short-lived higher excited states.

In this study, we developed PMI-coordinated CdS NCs (PMI-CdS) and ZnS NCs (PMI-ZnS Figure 1a), and investigated interfacial electron-transfer dynamics from higher excited states using transient absorption spectroscopy and pump-push-probe spectroscopy. We first focused on CdS NCs, which serve as effective probes of electron transfer, and then extended the study to ZnS NCs with a wider bandgap to examine how differences in acceptor energy levels and surface defects influence electron-transfer behavior. Furthermore, detailed analyses of the excited-state dynamics were performed using compound **1** (Figure 1a), which lacks a carboxylic acid moiety, as a reference system.

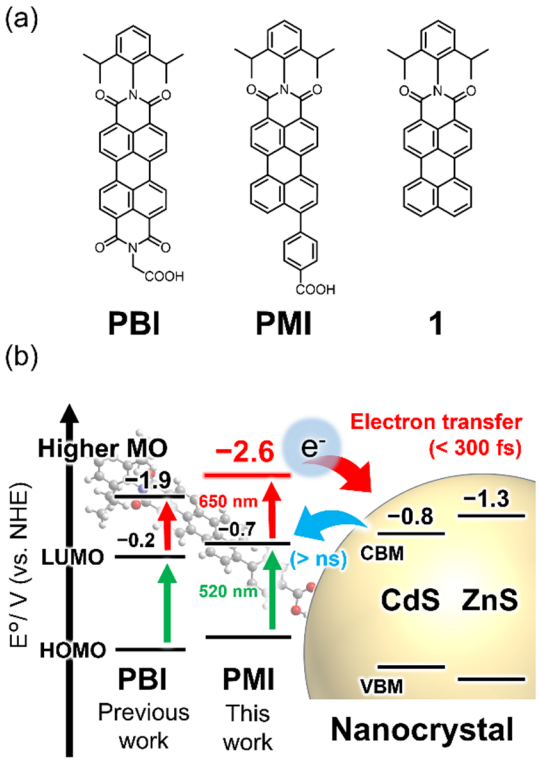

Figure 1. (**a**) Molecular structures of PBI, PMI, and compound **1**. (**b**) Schematic energy diagram of the stepwise two-photon-induced electron injection of PMI-CdS and PMI-ZnS. VBM and CBM indicate the valence band maximum and conduction band minimum, respectively.

Figure 1b schematically illustrates the concept of this study. Upon irradiation with a 520 nm pump pulse, PMI is excited to form the lowest singlet excited state (S_1). As described later, the S_1 of PMI exhibits a characteristic excited-state absorption band around 650 nm; therefore, irradiation with an additional 650 nm pulse within its lifetime enables the generation of a higher excited state (hereafter tentatively denoted as the S_n state). While S_n states conventionally undergo rapid nonradiative relaxation, we demonstrate that the extraction of the excited electron in S_n states to the conduction band minimum (CBM) of the NC allows the electron derived from this intrinsically short-lived higher excited state to survive for longer than nanoseconds. These findings expand the versatility of higher excited state chemistry using organic-inorganic nanohybrids and open new possibilities for the design of interfacial charge-transfer systems that effectively utilize high-energy electrons under mild optical conditions.

2. Results and Discussion

PMI, CdS NCs, and ZnS NCs were synthesized according to previously reported methods (see supporting information (SI) for details). X-ray diffraction (XRD) measurements reveal that the crystal structure of the synthesized CdS and ZnS NCs is zincblende (Figure S6). Transmission electron microscopy (TEM) measurements reveal that the average diameters of CdS and ZnS NCs are 4.9 ± 0.6 nm (Figures 2b and S10a) and 3.5 ± 0.6 nm (Figures S9 and S10b), respectively. The size of CdS NCs is consistent with that obtained from the first excitonic absorption peak (4.9 nm) [34]. PMI-CdS was prepared by mixing a chloroform solution of PMI (9.1×10^{-5} M) and CdS NCs (6.1×10^{-6} M), each measured using a microsyringe, followed by standing for 16 h. PMI-ZnS was also prepared at the same molar ratio. The number of PMI per NC (PMI/CdS and PMI/ZnS) was set to 15, which were estimated by the molar absorption coefficients of these compounds.

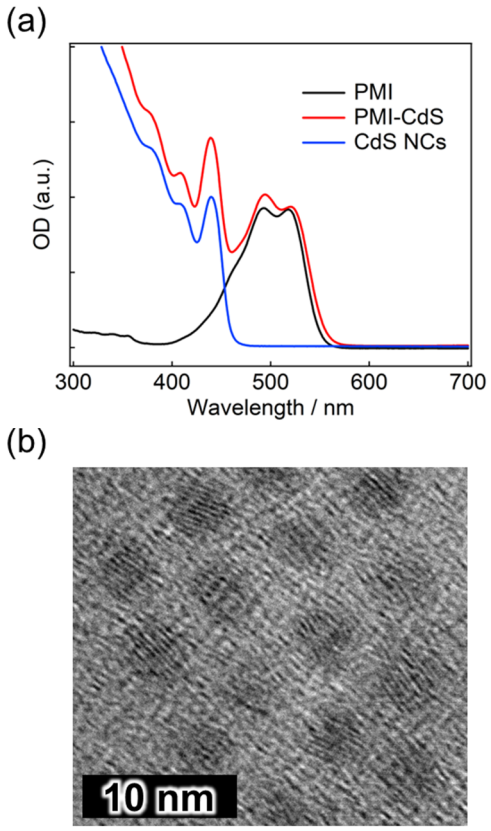

Figure 2. (**a**) Steady-state absorption spectra of PMI, CdS NCs, and PMI-CdS (the molar ratio: PMI/CdS = 15) in chloroform. (**b**) TEM image of CdS NCs.

The chloroform solution of PMI exhibits absorption peaks at 518 and 493 nm and a shoulder at 462 nm associated with vibronic progressions of the S_0–S_1 transition (Figure 2a). The chloroform solution of CdS NCs exhibits the first excitonic absorption peak at 440 nm. Upon coordination of PMI to CdS NCs, the absorption peaks derived from PMI are slightly red-shifted to 520 and 494 nm, accompanied by a broadening of the absorption bands. These spectral changes are attributed to the adsorption of PMI onto the surface of CdS NCs, as will be discussed in detail later based on fluorescence measurements. The molar absorption coefficient of the CdS NCs at the excitonic absorption peak is determined to be 8.3×10^5 M^{-1} cm^{-1} according to the previous report [34]. As described later, fluorescence measurements reveal that almost all PMI molecules are coordinated to CdS NCs in the concentration range of PMI/CdS ≤ 20. For comparison, similar red-shifted and band broadening were also observed for PMI-ZnS (Figures S8). ZnS NCs exhibit the first excitonic absorption peak at 307.5 nm (Figure S7), and the molar absorption coefficient of the ZnS sample is estimated to be 8.3×10^5 M^{-1} cm^{-1} at the excitonic absorption peak using the reported procedure [35,36].

To investigate the adsorption properties of PMI on CdS NCs in chloroform, fluorescence spectroscopy measurements were performed by stepwise addition of a CdS NC solution (6.1×10^{-5} M) to a chloroform solution of PMI with a fixed concentration of 1.0×10^{-6} M. In this approach, PMI/CdS decreases with increasing addition of the CdS NC solution. After each addition, the solution was allowed to stand for 10 min, followed by nitrogen

bubbling for 10 min, after which the fluorescence spectrum was recorded. The excitation wavelength was set at 488 nm. The fluorescence spectral changes at each PMI/CdS ratio, and the fluorescence peak wavelength as a function of the added concentration of CdS NCs are shown in Figure 3.

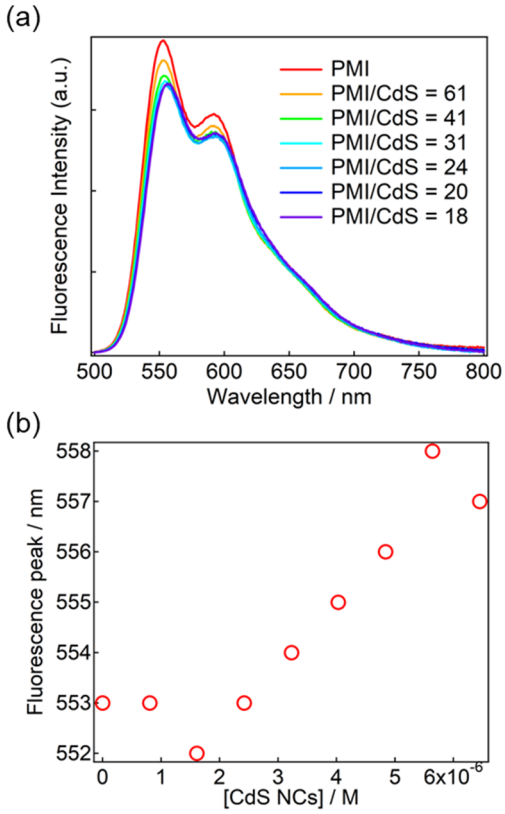

Figure 3. (**a**) Fluorescence spectra of PMI in $CHCl_3$ upon stepwise addition of CdS NCs under excitation at 448 nm and (**b**) Fluorescence peak maximum wavelength as a function of the added concentration of CdS NCs.

The chloroform solution of PMI exhibits a fluorescence maximum at 553 nm, with the fluorescence band extending to approximately 800 nm. Upon stepwise addition of the CdS NC solution (resulting in a gradual decrease in the PMI/CdS ratio), the fluorescence spectrum derived from PMI is shifted to the red, accompanied by a decrease in fluorescence intensity, which is attributable to the coordination of PMI to the surface of the CdS NCs. When the PMI/CdS ratio reaches 20, both the spectral shape and the fluorescence intensity become nearly constant, suggesting that almost all PMI molecules are coordinated to CdS NCs at this concentration ratio. Adsorption of PMI on the surface of the NCs was also confirmed by proton nuclear magnetic resonance (^{1}H NMR) spectroscopy (Figure S15), where the ligand-derived signals were broadened or became unobservable because of surface heterogeneity.

The relative fluorescence quantum yields (***Φ*F**) of PMI and PMI-CdS (PMI/CdS = 15) are determined to be 1.00 and 0.88, respectively, using rhodamine 6G as a standard [37]. Thus, the decrease in fluorescence quantum yield upon coordination is limited. As discussed later, the highest occupied molecular orbital (HOMO) level of PMI is more positive than the valence band edge of CdS NCs, whereas the lowest unoccupied molecular orbital (LUMO) level of PMI is more negative than the conduction band edge of CdS NCs. Therefore, when defect states of NCs are not taken into account, neither energy transfer nor electron transfer from the excited PMI to the CdS NCs is expected to occur when the PMI moiety is selectively excited. The absorption spectrum of PMI-CdS is nearly a simple superposition of those of PMI and CdS NCs, and coordination causes only a small decrease in the fluorescence quantum yield of PMI. These results indicate that the electronic interaction between the lowest excited state of PMI and CdS NCs is weak.

Potentials of the conduction and valence bands of ZnS relative to those of PMI suggest that neither electron transfer nor energy transfer occurs from the S_1 state of PMI. However, the relative fluorescence quantum yield of PMI-ZnS (PMI/ZnS = 15, ***Φ*F** = 0.62) is much lower than that of PMI and PMI-CdS. Because ZnS is known to form a higher density of defect states than CdS, the observed decrease in the relative fluorescence quantum yield is likely attributable to electron transfer via defect states, presumably associated with sulfur vacancies.

To clarify the excited-state dynamics of PMI and PMI-CdS in chloroform, femtosecond transient absorption measurements were performed. The excitation wavelength was set to 520 nm with a pulse energy of 30 nJ pulse^{-1} to selectively excite PMI. Figure 4 shows the transient absorption spectra and dynamics obtained after photoexcitation. To gain further insight into these dynamics, global analysis based on singular value decomposition was performed using the Glotaran program [38]. A three- or four-state sequential kinetic model convoluted with a Gaussian instrument response function was tentatively applied, and the transient absorption data were decomposed into three or four evolution-associated spectra (EAS1–EAS3 or EAS4). Details of the fitting procedure are provided in Figures S17–S19.

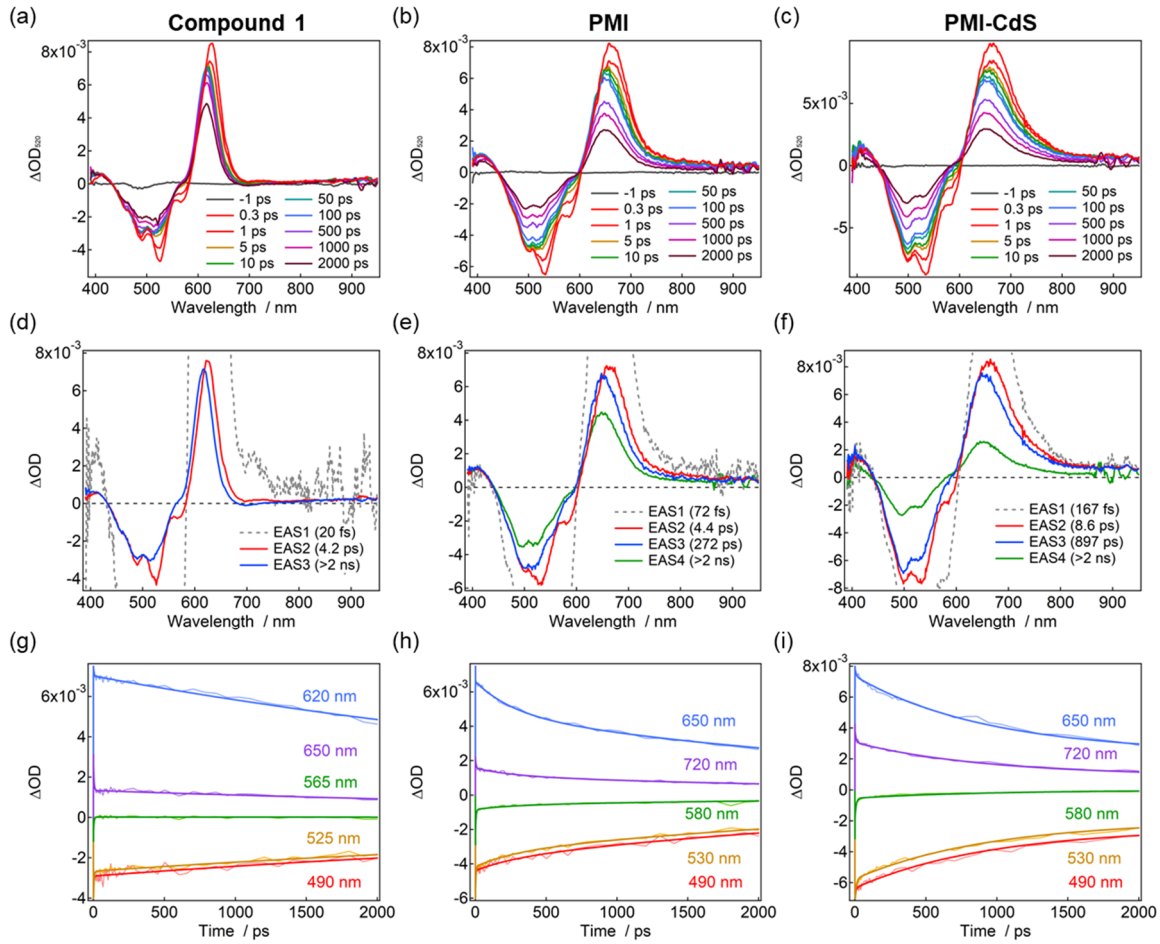

Figure 4. (**a**–**c**) Femtosecond to nanosecond transient absorption spectra, (**d**–**f**) evolution-associated spectra, and (**g**–**i**) dynamics of compound **1** (1.6×10^{-4} M), PMI (9.1×10^{-5} M), and PMI-CdS (PMI/CdS = 15) in $CHCl_3$ excited at 520 nm (30 nJ pulse^{-1}) at room temperature.

The excited-state dynamics of compound **1** in chloroform are first described as a reference (Figure 4a,d,g). EAS1, with time constants on the order of tens to a hundred femtoseconds, contains a significant contribution from the nonlinear optical response of the solvent and is therefore not discussed further in this study. EAS2 is characterized by distinct ground-state bleach and stimulated emission features together with a slight blue shift of the transient absorption band at 650 nm. Considering both its spectral evolution and picosecond timescale, the EAS2 is attributed to vibrational relaxation from the initially populated Franck–Condon state to the lowest vibrational level of the S_1 state. Subsequently, the S_1 state undergoes monoexponential relaxation on the nanosecond timescale.

PMI exhibits similar ultrafast components, with the solvent nonlinear response and vibrational relaxation appearing as EAS1 and EAS2, respectively (Figure 4b,e,h). In the transient absorption spectra of PMI, negative signals assigned to ground-state bleach and stimulated emission appear instantaneously at 498, 533, and 580 nm upon 520-nm excitation, while a positive band attributed to excited-state absorption is observed at 665 nm. This positive band shifts slightly to 650 nm within a few picoseconds, in good agreement with the assignment of EAS2 to the Franck–Condon state, which decays via vibrational relaxation. In addition to these components, PMI shows

an extra EAS3 component with a time constant of 272 ps. Comparison with compound **1** suggests that this component is associated with the carboxylic acid group of PMI. Diffusion-ordered spectroscopy (DOSY) measurements suggest that PMI molecules may form dimers in chloroform through intermolecular interactions between carboxylic acid groups (Figure S14). It should be noted that the PMI concentration employed in the transient absorption measurements was more than an order of magnitude higher than that used in the fluorescence measurements. Thus, the near-unity fluorescence quantum yield of PMI obtained under dilute conditions is not necessarily inconsistent with the contribution of intermolecular association under the present conditions. This effect may be reflected in the transient absorption response. Following EAS3, a nanosecond decay assigned to S_1 relaxation is observed as EAS4.

For PMI-CdS, the overall transient absorption spectra are similar to those of PMI (Figure 4c,f,i). The excited-state absorption band derived from PMI becomes slightly broader upon coordination to the CdS NC surface. On the other hand, the peak wavelength is nearly identical to that of PMI, suggesting that the broadening is likely due to inhomogeneity arising from differences in PMI's binding sites and binding modes on the NC surface. Consistent with these spectral features, the excited-state dynamics of PMI-CdS can also be decomposed into time-constant components, similar to those of PMI. However, the time constants of EAS2 and EAS3 are slightly longer than those of PMI. The slightly prolonged EAS2 and EAS3 components may reflect modification of the local environment around PMI upon coordination to the NC surface, where surrounding ligands such as oleic acid partially restrict molecular motion, thereby slowing vibrational relaxation and the reorientation dynamics associated with the carboxylic acid group. Similar spectral features and dynamics were also observed for PMI-ZnS (Figure S19). These results suggest that the electronic interaction between the S_1 state of PMI and the semiconductor NCs is weak in both PMI-CdS and PMI-ZnS.

Upon 347-nm excitation of PMI-CdS, where CdS NCs are predominantly excited, transient spectral features assignable to photoexcited CdS NCs were observed in the early time region (Figure S27). Subsequently, another set of signals, similar to those observed following direct excitation of PMI, gradually emerges on the tens-of-picoseconds timescale, suggesting the formation of PMI-derived transient species after excitation of the CdS NCs. Based on the HOMO and LUMO energy levels of PMI, together with the conduction- and valence-band edge potentials of the CdS NCs, these observations suggest that direct excitation of the CdS NCs induces energy or electron transfer to the PMI moiety. Further details are provided in the Supporting Information.

To investigate the dynamics of the higher excited states of PMI, PMI-CdS, and PMI-ZnS, pump-push-probe spectroscopy was employed, in which femtosecond transient absorption measurements were performed using two excitation pulses separated by a controlled time delay. The first pump pulse (P_1) was set to 520 nm with a pulse energy of 250 nJ pulse^{-1}. The second pump pulse (P_2) was set at 650 nm with a pulse energy of 80 nJ pulse^{-1} to further excite the S_1 of PMI to a higher excited state. In the present study, the delay time between P_1 and P_2 (t_{12}) was fixed at 5 ps, at which coherent effects are absent, and the vibrationally hot state has largely relaxed to the lowest excited state. The transient absorption changes associated with the higher excited state were expressed as ΔΔOD, which was obtained by subtracting the transient absorption signal induced by 520 nm excitation alone (ΔOD_{520}) from that induced by combined excitation with the 520 and 650 nm pulses ($\Delta OD_{520+650}$); that is, $\Delta\Delta OD = \Delta OD_{520+650} - \Delta OD_{520}$.

Figure 5a,b show the pump-push probe spectra and dynamics of PMI in chloroform excited with 520-nm and 650-nm excitation pulses. Immediately after excitation, pump-push-probe spectra of PMI exhibit a negative signal at 650 nm corresponding to depletion of the S_1 state, together with positive signals at 490, 550, and 580 nm, which are attributed to recovery of the ground-state bleach and a decrease in stimulated emission. These results suggest that PMI was promoted to higher excited states.

The positive signals associated with stimulated emission are larger than those of the ground-state bleaches. The stimulated emission decays rapidly within 1 ps, and the observed spectrum becomes nearly the inverse of that obtained under 520 nm pump-only excitation. Importantly, the inverse spectrum persists beyond nanoseconds, while the signals gradually decay to the initial state, i.e., the S_1 state. Because higher excited states generally decay to the lowest excited state within 1 ps, the nanosecond dynamics observed here cannot reasonably be attributed to relaxation from the higher excited state itself. Even if electron transfer or ionization from the higher excited state were to produce another transient reactive species, such as radicals, such a process should give rise to distinct spectral signatures beyond a mere inversion of the S_1 spectrum, and it would not naturally account for the eventual recovery to the original S_1 state. These considerations strongly suggest that the anomalous long-lived component is not due to a genuine photoproduct formed in the higher excited state, but rather to an apparent population change of the S_1 state.

In fact, a simple two-state analysis of ΔΔOD demonstrates that, when the S_1 population is reduced by stimulated emission, the S_1 lifetime component is intrinsically embedded in the ΔΔOD response (details are

described in the SI). In the previously reported PBI-CdS system [32], this effect was not pronounced because the P_2 wavelength was set at 705 nm, although a weakly related feature was observed for PBI alone and was not discussed further. In the present system, however, the P_2 pulse wavelength is 650 nm, much closer to the fluorescence band, and this contribution therefore becomes much more significant.

To isolate the dynamics of the higher excited state more selectively, the transient absorption dynamics obtained under P_1-only excitation were scaled by an appropriate factor (α) so that their slow decay component matched that observed in the ΔΔOD dynamics, and the resulting scaled single-pulse transient absorption spectra were then subtracted from the two-pulse data ($\Delta\Delta\Delta OD = \Delta\Delta OD_{520+650} - \alpha\Delta OD_{520}$). At 650 nm, corresponding to the maximum of the transient absorption band of PMI, the slow decay components obtained under one-pulse and two-pulse excitation coincide remarkably well (Figure 5c). The good agreement of these slow dynamics suggests that the long-lived component predominantly reflects the decay of the S_1 state rather than the intrinsic dynamics of the higher excited state. We therefore newly define ΔΔΔOD as the difference between the two-pulse signal and the scaled single-pulse transient absorption signal, and use this quantity to reexamine the higher excited-state dynamics.

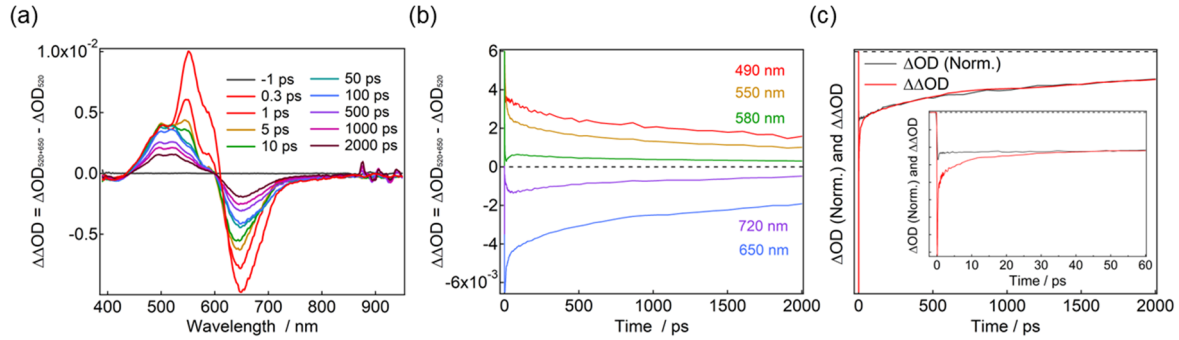

Figure 5. (**a**) Pump-push-probe spectra and (**b**) dynamics of PMI in chloroform excited by a 520 nm P_1 pulse (250 nJ pulse^{-1}) and a 650 nm P_2 pulse (80 nJ pulse^{-1}). The delay between P_1 and P_2 (t_{12}) was fixed at 5 ps. Time zero was defined as the moment when the P_2 pulse and the probe pulse arrived at the sample simultaneously. (**c**) Comparison of the decay profiles of the pump-push-probe dynamics and the one-pulse transient absorption dynamics probed at 650 nm. The decay trace obtained with 520 nm excitation alone was normalized to the long-time decay component.

Figure 6a,d,g present the subtracted pump-push-probe spectra (ΔΔΔOD), the corresponding EAS, and the time profiles at several probe wavelengths for PMI. After subtraction of the nanosecond-lived component arising from stimulated emission, the spectral changes associated with S_1 depletion and S_n formation are revealed much more clearly. Following EAS1, assigned to the nonlinear solvent response, EAS2 (811 fs) and EAS3 (11 ps) appear. Based on their spectral characteristics and time constants, EAS2 and EAS3 are attributed to the Franck-Condon state of S_n states and the subsequent relaxation of their vibrationally hot states, respectively. EAS4 (553 ps) shows a spectral shape slightly different from that of S_1. Because this component is too slow to be assigned to relaxation from the higher excited state, it may reflect an additional process arising from PMI aggregation. EAS5 (>2 ns), although extremely weak, may represent a transient photoproduct formed only under double-pulse excitation, as discussed in the following paragraph.

For PMI-CdS (Figure 6b,e,h), in addition to the ΔΔΔOD spectral components observed for PMI, an additional negative signal and a positive signal were observed around 440 and 460 nm, respectively. Because no such features were generated upon excitation at 650 nm alone, these signals are assigned to excited-state species on the CdS NCs generated via the higher excited state of PMI. These signals are clearly smaller than those produced by direct excitation of CdS, and the positive component is relatively more pronounced. This suggests that the spectral profile is distorted into a derivative-like shape by effects such as the carrier-induced Stark effect, leading to an apparent underestimation of the bleach amplitude. The CdS bleach signal was generated instantaneously upon excitation and persisted for longer than nanoseconds (Figure 6h). This indicates that the charge-separated state generated by sequential excitation with the 520 and 650 nm pulses is long-lived.

Further insight can be obtained by comparing the shapes and time constants of the EAS derived from global analysis. In the early-time component, EAS2 exhibits a spectral shape broadly similar to that of PMI; however, the time constant (740 fs) is almost the same or slightly shorter than that of PMI. This very slight acceleration of the decay may suggest the contribution of ultrafast charge injection into CdS NCs. For EAS3 and EAS4, the band

around 510 nm becomes relatively more pronounced. EAS4 (134 ps) exhibits an inverted spectral shape relative to the S_1 signal, indicating that the system has not yet fully returned to the original S_1 state on this timescale. Furthermore, EAS5 (>2 ns) displays a distinct positive signal in the 560–600 nm region, although these signals are very small. This spectral profile of EAS5 closely resembles that reported for the PMI radical anion [39]. These results suggest that an electron is first injected from the higher excited state of PMI into the CdS NC and is subsequently transferred to another PMI molecule coordinated on the same NC surface, thereby spatially separating the electron from the initially oxidized PMI and suppressing direct back electron transfer. Such a cooperative process involving multiple chromophores has also been reported previously for the PBI-CdS system [32]. In addition, because the CdS bleach-like signal persists for a long time, it is likely that the hole initially left on PMI is transferred to, or redistributed within, the CdS side on a certain timescale.

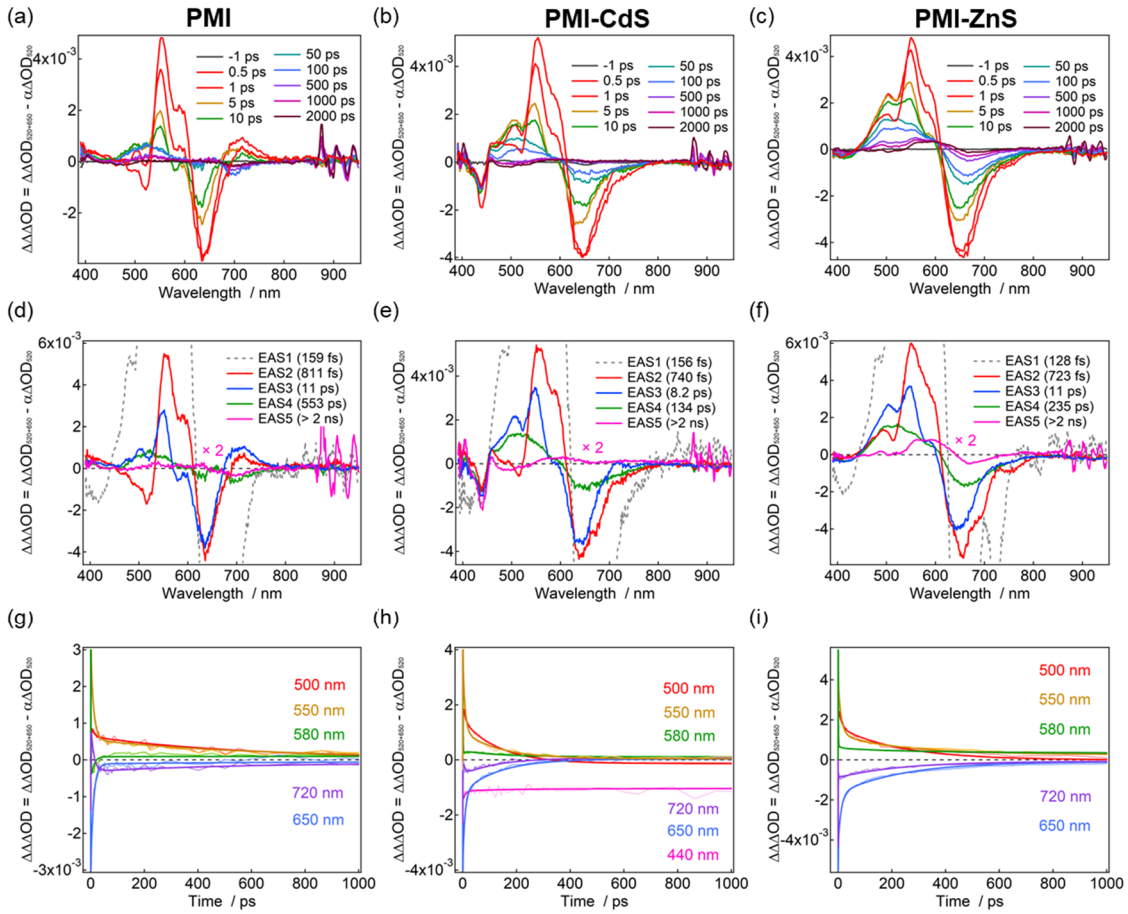

Figure 6. (**a**–**c**) Subtracted pump-push-probe (ΔΔΔOD) spectra, (**d**–**f**) evolution-associated spectra (EAS), and (**g**–**i**) dynamics of PMI (9.1×10^{-5} M), PMI-CdS (PMI/CdS = 15), PMI-ZnS (PMI/ZnS = 15) in $CHCl_3$ excited at 520 nm (250 nJ pulse^{-1}) and 650 nm (80 nJ pulse^{-1}) with t_2 = 5 ps at room temperature.

A similar set of signals was also observed for PMI-ZnS (Figure 6c,f,i). As in PMI-CdS, EAS2 (723 fs), which probably indicates the higher excited states, exhibits almost the same or slightly shorter time constant than that of PMI. These time constants of EAS4 are nearly twice as long in ZnS NCs as in CdS NCs. A slower return of the electron to the original PMI increases the probability that the electron is instead transferred to another PMI molecule during this interval. Consistent with this interpretation, the EAS5 component, which is assignable to the PMI radical anion, is more than twice as intense in PMI-ZnS as in PMI-CdS. In general, the probability of intermolecular electron transfer to another PMI should increase with the number of PMI molecules coordinated per NC. However, because the PMI/NC ratios are comparable for the CdS and ZnS systems (PMI/CdS = PMI/ZnS = 15), the observed difference is unlikely to arise simply from the number of PMI molecules bound to each NC.

One possible explanation is that PMI-ZnS exhibits a clearly lower fluorescence quantum yield than PMI-CdS, suggesting that ZnS NCs contain a higher density of trap sites, most likely associated with zinc vacancies. If such trap states efficiently capture the hole [40,41], the driving force for electron return to the original PMI is reduced. This would slow the recovery represented by EAS4 relative to PMI-CdS, and increase the probability of

electron transfer to another PMI molecule coordinated on the same NC surface, which results in the efficient formation of the PMI radical anion. These results demonstrate that further excitation of the S_1 state of PMI with 650 nm light enables charge injection even into wide-bandgap ZnS NCs. Compared with the previously reported PBI-CdS system, the PMI used in the present study bears the carboxylic acid substituent through a phenyl spacer, which should result in a longer effective distance from the NC surface. Nevertheless, by introducing the new analysis based on further subtraction from ΔΔOD, we successfully revealed electron transfer from the higher excited state across a π-conjugated organic ligand-NC interface. Moreover, the present results suggest that appropriate suppression of back electron transfer, for example by exploiting defect states in NCs, may provide a route to more efficient generation of the PMI radical anion, namely, a long-lived charge-separated state.

3. Conclusions

In summary, pump-push-probe spectroscopy revealed that higher excited states of PMI coordinated to CdS and ZnS NCs can rapidly inject electrons into the NCs, leading to long-lived charge-separated states. While the lowest excited state of PMI shows only weak electronic interaction with the NC surface, sequential excitation with 520 and 650 nm pulses opens an efficient pathway for interfacial electron transfer from higher excited states. The modified subtraction analysis introduced in this study enabled us to distinguish the intrinsic higher excited-state dynamics from the long-lived stimulated-emission contribution. In particular, PMI-ZnS shows more efficient formation of the PMI radical anion, suggesting that suppression of back electron transfer by trap states plays an important role. These results extend the strategy of utilizing short-lived higher excited states from PBI-based systems to PMI–nanocrystal hybrids and provide insight into the design of visible-light-driven charge-transfer systems using high-energy excited states.

Supplementary Materials

The additional data and information can be downloaded at: https://media.sciltp.com/articles/others/260605110 5231697/PSA-26040134-SI.pdf. Details of material characterizations, experimental setups, and time-resolved spectroscopies are provided in the Supporting Information.

Author Contributions

M.S.: investigation, data curation, formal analysis, writing—original draft preparation; D.Y.: investigation, methodology, formal analysis; H.S.: methodology, resources, investigation; Y.N.: investigation, methodology; Y.K.: conceptualization, supervision, funding acquisition, writing—review and editing. All authors have read and agreed to the published version of the manuscript.

Funding

This work was supported by JST, PRESTO Grant Number JPMJPR22N6, JSPS KAKENHI Grant Numbers JP24K01460, JP26K01461, JP23H04877, JP24K17749, JPMJAX25DF, and JP25H01687 (Transformative Research Areas (A) “Supra-ceramics”).

Institutional Review Board Statement

Not applicable.

Informed Consent Statement

Not applicable.

Data Availability Statement

The data that support the findings of this study are available from the corresponding author upon reasonable request.

Acknowledgments

The authors thank the staff of the Ritsumeikan University Research Organization for technical support and fruitful discussions.

Conflicts of Interest

The authors declare no conflict of interest.

Use of AI and AI-Assisted Technologies

During the preparation of this work, the authors used ChatGPT to assist with English language editing, including improvements to grammar, clarity, and readability. After using this tool, the authors reviewed and edited the content as needed and take full responsibility for the content of the published article.

References

1. Weinstain, R.; Slanina, T.; Kand, D.; et al. Visible-to-NIR-Light Activated Release: From Small Molecules to Nanomaterials. *Chem. Rev.* **2020**, *120*, 13135–13272. https://doi.org/10.1021/acs.chemrev.0c00663.
2. Yang, M.Q.; Gao, M.; Hong, M.; et al. Visible-to-NIR Photon Harvesting: Progressive Engineering of Catalysts for Solar-Powered Environmental Purification and Fuel Production. *Adv. Mater.* **2018**, *30*, 1802894. https://doi.org/10.1002/adma.201802894.
3. Mavridi-Printezi, A.; Menichetti, A.; Guernelli, M.; et al. Extending Photocatalysis to the Visible and NIR: The Molecular Strategy. *Nanoscale* **2021**, *13*, 9147–9159. https://doi.org/10.1039/d1nr01401c.
4. Pfund, B.; Wenger, O.S. Excited Organic Radicals in Photoredox Catalysis. *JACS Au* **2025**, *5*, 426–447. https://doi.org/10.1021/jacsau.4c00974.
5. Glaser, F.; Kerzig, C.; Wenger, O.S. Multi-Photon Excitation in Photoredox Catalysis: Concepts, Applications, Methods. *Angew. Chem. Int. Ed.* **2020**, *59*, 10266–10284. https://doi.org/10.1002/anie.201915762.
6. Kobayashi, Y.; Mutoh, K.; Abe, J. Stepwise Two-Photon Absorption Processes Utilizing Photochromic Reactions. *J. Photochem. Photobiol. C Photochem. Rev.* **2018**, *34*, 2–28. https://doi.org/10.1016/j.jphotochemrev.2017.12.006.
7. Zeng, L.; Huang, L.; Huang, Z.; et al. Long Wavelength Near-Infrared and Red Light-Driven Consecutive Photo-Induced Electron Transfer for Highly Effective Photoredox Catalysis. *Nat. Commun.* **2024**, *15*, 7270. https://doi.org/10.1038/s41467-024-50795-y.
8. Fang, Y.; Liu, T.; Chen, L.; et al. Exploiting Consecutive Photoinduced Electron Transfer (ConPET) in CO2 Photoreduction. *Chem. Commun.* **2022**, *58*, 7972–7975. https://doi.org/10.1039/d2cc02356c.
9. Gong, H.X.; Cao, Z.; Li, M.H.; et al. Photoexcited Perylene Diimide Radical Anions for the Reduction of Aryl Halides: A Bay-Substituent Effect. *Org. Chem. Front.* **2018**, *5*, 2296–2302. https://doi.org/10.1039/c8qo00445e.
10. Cao, Q.; Feng, J.; Fan, K.; et al. Extreme Potential Photocatalysis Enabled by Spin-Exchange Auger Processes in Magnetic-Doped Quantum Dots. *Nat. Commun.* **2025**, *16*, 5280. https://doi.org/10.1038/s41467-025-60659-8.
11. Barkeshli, M.; Berg, E.; Kivelson, S. Coherent transmutation of electrons into fractionalized anyons. *Science* **2014**, *346*, 722–725. https://doi.org/10.1126/science.1253251.
12. Zeman, C.J.; Kim, S.; Zhang, F. Direct Observation of the Reduction of Aryl Halides by a Photoexcited Perylene Diimide Radical Anion. *J. Am. Chem. Soc* **2020**, *142*, 2204–2207. https://doi.org/10.1021/jacs.9b13027.
13. Porte, N.T.; Martinez, J.F.; Hedström, S. Photoinduced Electron Transfer from Rylenediimide Radical Anions and Dianions to $Re(Bpy)(CO)_3$ Using Red and near-Infrared Light. *Chem. Sci.* **2017**, *8*, 3821–3831. https://doi.org/10.1039/c6sc05103k.
14. Inagaki, Y.; Mutoh, K.; Abe, J. Stepwise Photochromism of Bisnaphthopyrans Exhibiting an Excitation Intensity-Dependent Color Change. *Photochem. Photobiol. Sci.* **2018**, *17*, 946–953. https://doi.org/10.1039/c8pp00205c.
15. Ward, C.L.; Elles, C.G. Controlling the Excited-State Reaction Dynamics of a Photochromic Molecular Switch with Sequential Two-Photon Excitation. *J. Phys. Chem. Lett.* **2012**, *3*, 2995–3000. https://doi.org/10.1021/jz301330z.
16. Fu, Y.; Wang, J.; Zhang, Y. A Femtosecond Optical Switch Using Molecular Two-Photon Absorption with Multi-Step Charge Dissociation. *J. Mater. Chem. C Mater* **2022**, *10*, 6812–6817. https://doi.org/10.1039/d2tc00062h.
17. Mutoh, K.; Kobayashi, Y.; Yamane, T. Rate-Tunable Stepwise Two-Photon-Gated Photoresponsive Systems Employing a Synergetic Interaction between Transient Biradical Units. *J. Am. Chem. Soc* **2017**, *139*, 4452–4461. https://doi.org/10.1021/jacs.6b13322.
18. Yanai, N.; Kimizuka, N. New Triplet Sensitization Routes for Photon Upconversion: Thermally Activated Delayed Fluorescence Molecules, Inorganic Nanocrystals, and Singlet-to-Triplet Absorption. *Acc. Chem. Res.* **2017**, *50*, 2487–2495. https://doi.org/10.1021/acs.accounts.7b00235.
19. Schulze, T.F.; Czolk, J.; Cheng, Y.Y.; et al. Efficiency Enhancement of Organic and Thin-Film Silicon Solar Cells with Photochemical Upconversion. *J. Phys. Chem. C* **2012**, *116*, 22794–22801. https://doi.org/10.1021/jp309636m.
20. Ravetz, B.D.; Pun, A.B.; Churchill, E.M.; et al. Photoredox Catalysis Using Infrared Light via Triplet Fusion Upconversion. *Nature* **2019**, *565*, 343–346. https://doi.org/10.1038/s41586-018-0835-2.

21. Liu, Q.; Xu, M.; Yang, T.; et al. Highly Photostable Near-IR-Excitation Upconversion Nanocapsules Based on Triplet-Triplet Annihilation for in Vivo Bioimaging Application. *ACS Appl. Mater. Interfaces* **2018**, *10*, 9883–9888. https://doi.org/10.1021/acsami.7b17929.
22. Regehly, M.; Garmshausen, Y.; Reuter, M.; et al. Xolography for Linear Volumetric 3D Printing. *Nature* **2020**, *588*, 620–624. https://doi.org/10.1038/s41586-020-3029-7.
23. Hahn, V.; Messer, T.; Bojanowski, N.M.; et al. Two-Step Absorption Instead of Two-Photon Absorption in 3D Nanoprinting. *Nat. Photonics* **2021**, *15*, 932–938. https://doi.org/10.1038/s41566-021-00906-8.
24. Bojanowski, N.M.; Vranic, A.; Hahn, V.; et al. Search for Alternative Two-Step-Absorption Photoinitiators for 3D Laser Nanoprinting. *Adv. Funct. Mater.* **2023**, *33*, 2212482. https://doi.org/10.1002/adfm.202212482.
25. Livache, C.; Kim, W.D.; Jin, H.; et al. High-Efficiency Photoemission from Magnetically Doped Quantum Dots Driven by Multi-Step Spin-Exchange Auger Ionization. *Nat. Photonics* **2022**, *16*, 433–440. https://doi.org/10.1038/s41566-022-00989-x.
26. Koga, M.; Yoneda, Y.; Sotome, H.; et al. Ionization Dynamics of a Phenylenediamine Derivative in Solutions as Revealed by Femtosecond Simultaneous and Stepwise Two-Photon Excitation. *Phys. Chem. Chem. Phys.* **2019**, *21*, 2889–2898. https://doi.org/10.1039/c8cp06530f.
27. Sotome, H.; Koga, M.; Sawada, T.; et al. Femtosecond Dynamics of Stepwise Two-Photon Ionization in Solutions as Revealed by Pump-Repump-Probe Detection with a Burst Mode of Photoexcitation. *Phys. Chem. Chem. Phys.* **2022**, *24*, 14187–14197. https://doi.org/10.1039/d1cp03866d.
28. Kasha, M. Characterization of electronic tran- sitions in complex molecules. *Discuss. Faraday Soc.* **1950**, *9*, 14–19. https://doi.org/10.1039/df9500900014.
29. Del Valle, J.C.; Catalán, J. Kasha's Rule: A Reappraisal. *Phys. Chem. Chem. Phys.* **2019**, *21*, 10061–10069. https://doi.org/10.1039/c9cp00739c.
30. Tisdale, W.A.; Williams, K.J.; Timp, B.A. Hot-Electron Transfer from Semiconductor Nanocrystals. *Science* **1979**, *328*, 1543–1547. https://doi.org/10.1126/science.1185509.
31. Zhao, Z.; Niu, F.; Li, P. Visible Light Generation of a Microsecond Long-Lived Potent Reducing Agent. *J. Am. Chem. Soc.* **2022**, *144*, 7043–7047. https://doi.org/10.1021/jacs.2c00422.
32. Yoshioka, D.; Fukuda, D.; Kobayashi, Y. Green and Far-Red-Light Induced Electron Injection from Perylene Bisimide to Wide Bandgap Semiconductor Nanocrystals with Stepwise Two-Photon Absorption Process. *Nanoscale* **2021**, *13*, 1823–1831. https://doi.org/10.1039/d0nr08493j.
33. Xu, Y.; Zheng, J.; Lindner, J.O. Consecutive Charging of a Perylene Bisimide Dye by Multistep Low-Energy Solar-Light-Induced Electron Transfer Towards H2 Evolution. *Angew. Chem. Int. Ed.* **2020**, *59*, 10363–10367. https://doi.org/10.1002/anie.202001231.
34. Yu, W.W.; Qu, L.; Guo, W.; et al. Experimental Determination of the Extinction Coefficient of CdTe, CdSe, and CdS Nanocrystals. *Chem. Mater.* **2003**, *15*, 2854–2860. https://doi.org/10.1021/cm034081k.
35. Yoshioka, D.; Yoneda, Y.; Chang, I.Y.; et al. Quasi-Reversible Photoinduced Displacement of Aromatic Ligands from Semiconductor Nanocrystals. *ACS Nano* **2023**, *17*, 11309–11317. https://doi.org/10.1021/acsnano.2c12578.
36. Maes, J.; Balcaen, L.; Drijvers, E.; et al. Light Absorption Coefficient of CsPbBr3 Perovskite Nanocrystals. *J. Phys. Chem. Lett.* **2018**, *9*, 3093–3097. https://doi.org/10.1021/acs.jpclett.8b01065.
37. Würth, C.; Grabolle, M.; Pauli, J.; et al. Relative and Absolute Determination of Fluorescence Quantum Yields of Transparent Samples. *Nat. Protoc.* **2013**, *8*, 1535–1550.
38. Snellenburg, J.J.; Laptenok, S.; Seger, R.; et al. Glotaran: A Java-based graphical user interface for the R package TIMP. *J. Stat. Softw.* **2012**, *49*, 1–22.
39. Gosztola, D.; Niemczyk, M.P.; Svec, W.; et al. Excited Doublet States of Electrochemically Generated Aromatic Imide and Diimide Radical Anions. *J. Phys. Chem. A* **2000**, *104*, 6545–6551. https://doi.org/10.1021/jp000706f.
40. Xiao, B.; Lv, T.; Zhao, J.; et al. Synergistic Effect of the Surface Vacancy Defects for Promoting Photocatalytic Stability and Activity of ZnS Nanoparticles. *ACS Catal.* **2021**, *11*, 13255–13265. https://doi.org/10.1021/acscatal.1c03476.
41. Hao, X.; Wang, Y.; Zhou, J. Zinc Vacancy-Promoted Photocatalytic Activity and Photostability of ZnS for Efficient Visible-Light-Driven Hydrogen Evolution. *Appl. Catal. B* **2018**, *221*, 302–311. https://doi.org/10.1016/j.apcatb.2017.09.006.